Visualization of Atomic-Scale Motions in Materials via Femtosecond X-Ray Scattering Techniques

Aaron M. Lindenberg,[1,2] Steven L. Johnson,[3] and David A. Reis[2,4]

[1]Department of Materials Science and Engineering, Stanford University, Stanford, California 94305; email: aaronl@stanford.edu

[2]Department of Photon Science, Stanford University and SLAC National Accelerator Laboratory, Menlo Park, California 94025

[3]Institute for Quantum Electronics, Physics Department, ETH Zürich, 8093 Zürich, Switzerland

[4]Department of Applied Physics, Stanford University, Stanford, California 94305

Annu. Rev. Mater. Res. 2017. 47:425–49

First published as a Review in Advance on April 7, 2017

The *Annual Review of Materials Research* is online at matsci.annualreviews.org

https://doi.org/10.1146/annurev-matsci-070616-124152

Keywords

ultrafast materials science, X-ray scattering, imaging, light-matter interactions, phase transitions, dynamics

Abstract

We review current progress with respect to ultrafast, atomic-scale resolution X-ray scattering studies of materials. In the last decade, advances in sources and techniques have opened up new possibilities for probing the dynamics of how materials change in situ and in real time. These developments have enabled direct measurements of the first primary steps in how complex/functional materials transform and the flow of energy between different degrees of freedom. Unique insight into the mechanisms underlying how materials function is obtained through these studies. An outlook on future developments and new opportunities is also presented.

1. INTRODUCTION

FEL: free-electron laser

Atomic-scale motions in materials occur across a vast range of timescales and length scales. Our understanding of these processes is shaped by our ability to probe them, and over the past century, a range of approaches have been adapted to try to visualize how atoms are moving. For example, in the frequency domain, optical techniques such as infrared or Raman spectroscopy are sensitive to vibrational degrees of freedom and can extract important structural information. Over the last several decades, significant efforts have been made to go beyond these more indirect approaches and to develop means to reconstruct the structure of materials at atomic-scale resolution as they are evolving. This means extending basic techniques such as X-ray crystallography, as often applied to measure frozen-in structures of biologically relevant molecules, to extract the intermediate states and mechanistic pathways that the molecules pass through as they transform (i.e., not just reactant and product states) (1). In the realm of materials science and solid-state physics on which this review is focused, direct information concerning how atoms are moving and how unit cells are deforming and reconfiguring can be obtained through these approaches, despite the fact that the timescale for these dynamics can be as fast as a few tens of femtoseconds (10^{-15} s), comparable to the period of the highest-frequency optical phonons. For example, the original fruit fly of femtosecond X-ray experiments concerned the study of bismuth crystals, where time-dependent measurements of the X-ray structure factor enable direct measurement of the unit cell deformations associated with the A_{1g} phonon mode and the Peierls distorted structure (2, 3). Since these early days, sources have improved by many orders of magnitude in brightness (4), and the range of materials systems that can be studied and the information that may be gleaned have been extended to encompass a vastly larger phase space.

This review summarizes the current status of the field, covering some of the pioneering experiments and the new understanding they have enabled concerning materials functionality. In so doing, we also provide a detailed outlook and summary of future directions as well as areas in which femtosecond scattering techniques may be significantly impactful within the broad field of materials science. We focus on experiments using X-ray scattering approaches only, leaving out approaches based on X-ray spectroscopy, electron diffraction, and so forth whose inclusion would make this review intractable under current length limits. Furthermore, this review is largely focused on the first experiments enabled by hard-X-ray free-electron lasers (FELs), which are revolutionizing this field, although a brief historical perspective is provided, and many of the early experiments making use of other sources are briefly discussed. We focus further on examples in which the atoms are moving. This focus neglects a range of powerful techniques and experiments probing electronic or magnetic degrees of freedom.

2. OVERVIEW OF SOURCES AND TECHNIQUES

Because most X-ray detectors are not capable of intrinsically resolving subpicosecond timescales, the vast majority of femtosecond time-resolved measurements are performed in a pump-probe scheme, which we briefly describe here in a general way. The pump pulse here is some kind of perturbation to a material that initiates some particular dynamics that are under investigation. The probe is in this case a short, <100-fs-duration X-ray pulse that scatters from the material over a time interval that is short compared with the timescale of the changes in the structure. Both the pump and probe pulses are synchronized in time up to a controllable delay, although significant timing jitter often requires shot-by-shot determination of the relative delay and postprocessing to achieve the highest resolution (5, 6) (see sidebar titled Shot-by-Shot Timing Measurements). The scattered intensity from the probe pulse is measured, giving information about the instantaneous structure of the material at that time. This is done repeatedly both to accumulate statistics and

SHOT-BY-SHOT TIMING MEASUREMENTS

Because pump and probe pulses are typically generated by independent sources at X-ray FELs, there is often significant timing jitter/fluctuations (of the order of hundreds of femtoseconds). In this situation, auxiliary diagnostic experiments are often used to measure precisely the timing difference between particular pairs of pulses, which allows for postsorting data by actual arrival time at the experiment so that the overall time resolution of the experiment is uncompromised. In these auxiliary experiments, the roles of pump and probe are often reversed relative to the main experiment. A frequently encountered case is one in which the arrival time of the X-ray beam must be compared with that of a conventional femtosecond laser system that operates in or near the visible part of the spectrum. One popular solution to this problem is to use a small portion of the X-ray pulse to transiently change the optical properties of a thin material. These changes are measured by the transmission or reflection of a spectrally chirped optical pulse derived from a split-off portion of the conventional laser system. Here chirped means simply that the pulse is stretched in time so that the arrival time of the pulse on the thin material varies over the fairly broad set of wavelengths that compose the femtosecond laser pulse. A spectrograph set to measure the pulse after interaction with the thin material can then probe the time-dependent reflectivity over a substantial temporal range in a single shot (6, 7). As an alternative to using chirped pulses, a similar outcome can be achieved using a cross-beam geometry (5, 8, 9). Shot-by-shot diagnostics are also used to correct for other types of uncontrolled fluctuations, most often related to the spectrum, intensity, and pointing of the beam.

to allow for variation in the timing between the two pulses. Between pairs of pulses, either the material is assumed to relax back to its initial state, or it is replaced with an effectively identical system. By making repeated measurements of the scattering from the probe pulses for various time delays, it is possible to construct a time-dependent description of how the X-ray scattering response changes with respect to the pump pulse.

The history of femtosecond X-ray pump-probe measurements has been driven largely by the availability of short-pulse X-ray sources with sufficiently high flux and short wavelengths to make such experiments feasible (10, pp. 371–422). One type of source that found early use relies on X-ray emission from laser-generated plasmas to create short bursts of X-rays with a wavelength determined by the strong emission lines of the material used to create the plasma (11–13). These sources can have a relatively short pulse duration and can generate many X-ray photons in one burst. The resulting X-rays, however, have a very large angular divergence, which sometimes poses a challenge to scattering measurements, in which precise knowledge of the momentum of the incoming X-rays is important. This difficulty can be partly overcome by optimizing the overall efficiency of X-ray generation. Alternatively, this divergence can be used to measure a broad range of scattering angles at the same time (14), and indeed this kind of source remains in active use (15, 16).

At the same time as when the first plasma sources became available, research groups began to exploit the bunched time structure of X-rays emitted from synchrotrons as well as ultrafast streak camera detectors (17) to perform time-resolved X-ray scattering experiments with picosecond resolution (18–20). These early efforts have now been extended at a number of synchrotrons to pump-probe measurements with much higher repetition rates, making use of the intrinsic high repetition rate of electron bunches in storage rings (21–23). The advent of the electron beam slicing technique (see sidebar titled Electron Beam Slicing) (24, 25) enabled truly femtosecond pump-probe measurements at synchrotrons by effectively reducing the normally >100-ps duration of the pulses to >100 fs, at the cost of a proportional amount of X-ray flux. After the technique's first demonstration at the Advanced Light Source in Berkeley, California, this approach was

Angular divergence: the spread of angles (both vertical and horizontal) in a propagating beam

ELECTRON BEAM SLICING

Performing pump-probe experiments with subpicosecond resolution at synchrotron light sources is normally difficult because stable operation of the electron storage ring requires fairly long electron bunches, typically on the order of 100 ps in duration for normal operation at most facilities. Electron beam slicing, a method first proposed by Zholents & Zolotorev (24) and demonstrated by Schoenlein et al. (25), uses an intense femtosecond near-infrared laser to modulate the energy of a short slice of electrons in a synchrotron storage ring. These modulated electrons, which have a temporal duration that matches that of the near-infrared laser, are then separated from the other electrons by magnetic fields and are used in a bending magnet or undulator to create 50–100-fs-duration X-ray pulses.

implemented at several different synchrotron sources (26–28). Parallel recent efforts have focused on shortening X-ray pulses at synchrotrons through manipulation of the trajectories of electrons within an electron bunch such that the longitudinal bunch length of the emitting electrons is directly shortened, termed low-α modes (21, 29, 30). This reduction in pulse duration is often obtained at the expense of a significant loss in bunch current.

Despite the availability of plasma and slicing sources, the low per-pulse flux and peak brilliance from such sources pose a strong limitation on the range of measurements that are feasible. Accelerator-based sources optimized for short-pulse generation can provide femtosecond-duration pulses with peak brilliances that are many orders of magnitude higher. Freed of the requirement to stably store electrons in a ring, linear accelerators can generate subpicosecond-duration electron pulses with fairly high current. This was used at the Subpicosecond Pulse Source (SPPS) at the SLAC National Accelerator Laboratory in Menlo Park, California, to generate X-rays as in a synchrotron. Such a linear accelerator source was used to perform X-ray scattering measurements with much higher statistics than for previous sources (31). Soon afterward, the Linac Coherent Light Source (LCLS), the first hard-X-ray FEL, was commissioned, also at SLAC (32). FEL sources use bright relativistic electron bunches from an accelerator as the gain medium in a lasing process, producing orders-of-magnitude-higher X-ray intensities in femtosecond pulse durations and with full transverse coherence. The resulting increase in brightness has enabled a wide variety of time-resolved X-ray scattering experiments that were previously impossible. Soon afterward, the SACLA FEL in Japan offered similar capabilities (33), and several other hard-X-ray FEL sources are currently under commissioning work in Germany (34), Korea (35), and Switzerland (36).

3. COHERENT STRUCTURAL DYNAMICS

Much of the early and ongoing fundamental work on femtosecond time-resolved X-ray scattering has focused on temporal coherences in structural dynamics induced by electromagnetic radiation. Such coherences are uniquely observable by time-resolved techniques, and the use of X-ray scattering offers quantitative information on the magnitude of such coherences and thus a measurement of certain types of couplings. In addition, the high momentum of X-ray radiation can in some cases give useful information about the wave vector of the coherences.

Here we consider two types of coherences that have been investigated using femtosecond X-ray scattering. The first are so-called coherent states, which are essentially first-order coherences in some type of displacement field. The second type are higher-order coherences, for example,

COHERENT STATE

A coherent state (37) is a solution of the quantum harmonic oscillator in which the uncertainties of the displacement and momentum are constant in time and equal to their values in the ground state. In a coherent state, the expectation values of the displacement and momentum coordinates change periodically in time with a phase difference of 90 degrees. In a sense, coherent states are the most classical-like solutions to the quantum harmonic oscillator problem, in that the dynamics of the expectation values of the coordinates follow precisely those of the classical solutions.

squeezed states, including those involving correlations of two or more different normal modes of the structure.

3.1. Coherent States in Condensed Matter

In the context of condensed matter systems, the term coherent excitation is broadly used to describe a time-dependent state similar to a coherent state of some quantized field, in analogy to the coherent states of quantum optics discussed by Glauber (37) (see sidebar titled Coherent State). Although a strict analogy to the coherence discussed by Glauber would require time-dependent oscillations of the relevant field variable with a minimum uncertainty, in practice, coherent excitation is often used to describe any state of a field variable in which the expectation value oscillates with a nonzero amplitude and with a definite phase with respect to some reference time. The term is meant to distinguish such motions from the incoherent dynamics associated with thermalized systems, in which the expectation value of the field is zero (but the field variance is nonzero).

To put this discussion on a less abstract footing, consider the specific case of the field of atomic displacements in a crystal in which the instantaneous position of every atom is represented by a displacement vector $\mathbf{u}^j(\mathbf{R})$ from its equilibrium position, where $\mathbf{R}$ is a vector describing a specific unit cell and j is an index running over the n basis atoms. Expressed in terms of the different vibrational modes $Q_{\mathbf{k}s}$ of the crystal,

$$\mathbf{u}^j(\mathbf{R}) = \frac{1}{\sqrt{N}} \sum_{\mathbf{k}s} Q_{\mathbf{k}s} \epsilon^j_{\mathbf{k}s} e^{i\mathbf{k}\cdot\mathbf{R}} + \text{h.c.}, \qquad 1.$$

where $\epsilon^j_{\mathbf{k}s}$ are the eigenvectors for the $3n$ phonon branches s with wavevector $\mathbf{k}$ belonging to the N allowed values in the first Brillouin zone (corresponding to the total number of unit cells) and h.c. denotes the hermitian conjugate. In this context, a coherent phonon is a state of the displacement field in which $\langle Q_{\mathbf{k}s} \rangle$ is nonzero and time dependent, oscillating with a frequency $\omega_{\mathbf{k}s}$ with a phase well defined with respect to an externally defined reference. Here the angle brackets could refer to either the quantum mechanical expectation value or a classical ensemble average.

This external reference is typically tied to some kind of sudden excitation of the system. For example, rapid heating of a material with a femtosecond laser pulse generates a strain wave that propagates away from interfaces, which is equivalent to a spectrum of coherent acoustic modes with a bandwidth limited by the speed of sound across the penetration depth (38). The resulting dynamics were resolved in the early days of time-resolved X-ray diffraction measurements as time-dependent modulations of the intensity of diffraction in the tails of Bragg lattice reflections (19, 39, 40), a kind of inelastic scattering discussed further below. Depending on the system, impulsive optical excitation might also produce phonons via a more direct coupling of electronic states to acoustic modes via deformation potential coupling (see sidebar titled

DEFORMATION POTENTIAL COUPLING

The deformation potential coupling is a type of electron-phonon coupling that arises from the dependence of electronic state energies on lattice strain. In short, if the energy of a particular electronic state changes when the lattice is compressed along a particular direction, this electronic state will couple to long-wavelength acoustic vibrational modes that compress the lattice along this direction. This term is normally used only to describe coupling between electronic states and longitudinal acoustic modes.

Deformation Potential Coupling). A careful analysis of the dynamics can measure the strength of both contributions (19, 41, 42).

In systems with a nontrivial unit cell basis, sudden excitation of electronic states with a femtosecond laser pulse can lead to the creation of coherent phonons in the optical branches via a similar electron-phonon coupling term in the system Hamiltonian (43–46). As is the case with acoustic phonons generated by near-optical laser excitation, momentum conservation conditions restrict the population of coherent phonons to those with wavelengths comparable to or longer than the absorption depth of the exciting radiation. Because these depths are usually long compared to the unit cell dimensions, these phonons are limited to a region very close to the center of the Brillouin zone [a notable exception is in the presence of disorder (46, 47)]. Because the dispersion of the optical branches is very small in this region, we can typically approximate the optical phonons thus generated as essentially a set of zone-center modes characterized by oscillating $\langle Q_{\mathbf{0}r}(t)\rangle$, where r runs over the subset of optical branches that are excited. These dynamics were seen in early time-resolved X-ray diffraction measurements as time-dependent oscillations of the intensity of particular diffraction peaks that have a structure factor sensitive to these modes, allowing for quantitative measurement of the dynamics and the underlying coupling driving the motion (2, 3, 48, 49). Typically, these are fully symmetric modes (A_{1g} or A_1 modes) that are relatively easy to excite via so-called displacive excitation mechanisms [displacive excitation of coherent phonons (DECPs)] (see sidebar titled Displacive Excitation) (43), although low-amplitude coherent phonons of lower-symmetry modes excited by a more impulsive mechanism have also been seen in X-ray diffraction (50). The generation mechanism of coherent phonons of different symmetries and their relationship to Raman scattering and DECPs are discussed in Reference 51.

All the foregoing examples have been experiments in which electronic excitation of a material drives structural dynamics via electron-phonon coupling. An alternative method for generating large populations of coherent excitations in electronically gapped materials is to couple in intense pulses of electromagnetic radiation with a center frequency close to that of a resonance, provided that resonance is electric dipole allowed. More recently, there has been strong interest in the driving of coherent phonons with infrared activity using lower-frequency electromagnetic radiation. This mechanism generally applies only to electronically gapped systems in which the gap energy

DISPLACIVE EXCITATION

DECP is a mechanism by which coherent phonons are created by a sudden shift in the effective quasi-equilibrium value of a vibrational coordinate that happens on a timescale much faster than the period of the associated vibrational mode. After the shift, the expectation value of the coordinate oscillates around the new quasi-equilibrium value with a cosine-like waveform and an amplitude equivalent to the magnitude of the shift.

is larger than the relevant phonon energy. In this case, a phonon-polariton mode is excited in the system, provided that the frequency of the driving radiation is close to the natural frequency of the bare phonon mode (52).

Infrared active mode: a vibrational mode with an electric dipole that can be excited in first order by a time-varying electric field

One potential application of driving large-amplitude coherent vibrational modes in crystals in materials science is the generation of transient electronic states via so-called nonlinear phononics (53–55). Here the idea is that a sufficiently large coherent amplitude of a specific mode can lead to a distortion of the lattice along other normal mode coordinates via an anharmonic coupling. In systems with inversion symmetry, one of the lowest-order couplings of an infrared active mode is to a displacement of a Raman active mode (53, 56, 57). This displaced Raman mode can, in turn, induce changes in the electronic structure of the material, which may, in particular cases of strongly correlated electron systems, drive electronic phase transitions. A recent series of experiments using time-resolved methods to measure the THz frequency optical conductivity in nonsuperconducting phases of several cuprates (58–61) and the conventional superconductor K_3C_{60} (62) after resonant excitation of an infrared active phonon appear to show evidence of features similar to those seen in the superconducting state, leading to the tantalizing idea that nonlinear phononics may transiently induce superconducting transport.

The possible structural basis of this interaction has been studied with femtosecond X-ray diffraction in the case of $YBa_2Cu_3O_{6.5}$ (63). In this system, strong excitation of a B_{1u} mode with 300-fs-duration pulses tuned to the resonance frequency of 670 cm^{-1} was previously observed to lead to transient changes of the THz frequency optical conductivity that correspond to those seen on the transition to the superconducting state, suggestive of enhanced interlayer superconducting coupling (58, 60). In the X-ray experiment, the displacive structural changes in the material are studied by making time-resolved measurements of the intensity of several selected Bragg peaks. Although the observed changes are very small (on the order of 0.3%), the data are favorably compared with a model that predicts strong displacive coupling to a set of 4 A_{1g} modes that lead to a decrease in the apical oxygen distance and to an increase in in-plane buckling of the Cu-O layers (see **Figure 1**). These changes in structure are, via density functional theory calculations, also shown to alter the hybridization of states near the Fermi energy and may be the determining factor in driving superconducting-like states in this system.

In systems in which other degrees of freedom are strongly coupled to atomic displacements, coherent excitations of a mixed character can be driven. One example is so-called electromagnons, which are generally described as electric-dipole active excitations of spin structure that are observed in some multiferroic systems, for example, $TbMnO_3$ (64). This perovskite manganite exhibits a series of low-temperature antiferromagnetic phase transitions, displaying multiferroicity at temperatures lower than 27 K (65, 66). In this state, the uncompensated Mn spins are ordered as a cycloid within the *bc* plane with a wave vector along the *b* direction that is incommensurate with the lattice. This magnetic structure induces a ferroelectric polarization enhanced by a small atomic displacement (67). Certain modes of deformation of this spin structure are dynamically coupled to an electric polarization, making these spin excitations electric dipole active via a displacement of the oxygen atoms (68, 69). The electromagnon excitations manifest spectrally as two wide absorption features in the infrared at 0.8 THz and 1.8 THz. A theoretical model of this system proposed by Mochizuki & Nagaosa (70) indicates that very strong excitation of the higher-energy electromagnon resonance can drive a persistent switching of the direction of the antiferromagnetic cycloid order along with the accompanying ferroelectric polarization on a timescale of only a few picoseconds.

The lower-amplitude limit of this special type of mixed coherent excitation was recently studied using resonant X-ray diffraction at the Mn L_2 edge (71). At this energy, the normally negligible scattering contributions from magnetic order are strongly enhanced, resulting in a strong

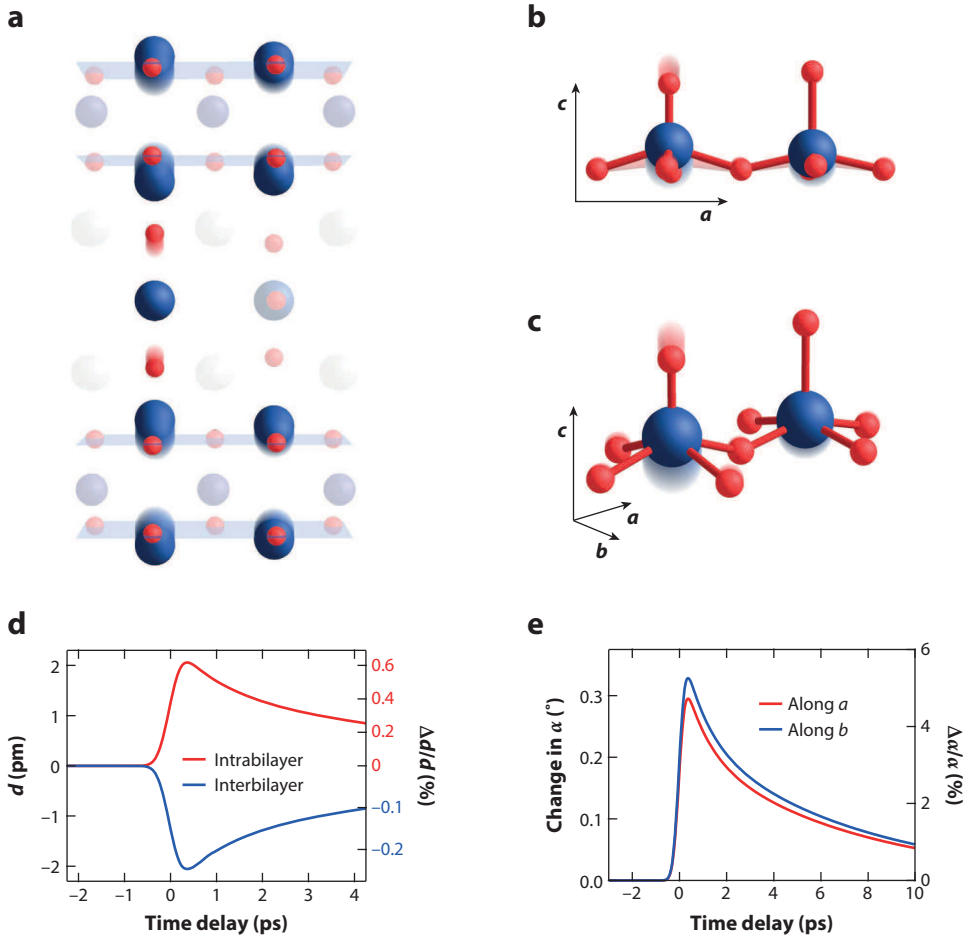

Figure 1

Suggested transient atomic displacements found to be consistent with measured time-dependent structure factor changes in $YBa_2Cu_3O_{6.5}$ resonantly excited at the B_{1u} phonon at 670 cm^{-1} (63). (*a–c*) Sketch of the transient displacement showing a decrease in the apical O-Cu distances by 2.4 pm at oxygen-deficient sites and an increase in O-Cu-O buckling. (*d*) The intrabilayer distance as a function of time. (*e*) The change in the in-plane buckling angle α along both *a* and *b*. Figure reprinted with permission from Reference 63.

diffraction peak at a position in reciprocal space corresponding to the magnetic ordering. The intensity of the peak is related to a magnetic structure factor that acts as a projection of the spin order. **Figure 2** shows the measured response, in comparison to the driving electric field at 1.8 THz. Analysis of the magnitude and character of the response suggests that the oscillating electric field induces a ±4° rotation of the plane of the cycloid spin order, which appears to be fully consistent with the expectations from the theory that predicts switching at THz field strengths that are approximately 10–20 times higher. The data also show, for the first time, a quantitative measurement of the spin part of a coherently driven electromagnon.

3.2. Higher-Order Coherences

The experiments described above correspond to structural changes associated with the long-range order of the sample. In these cases, density fluctuations corresponding to phonons reduce

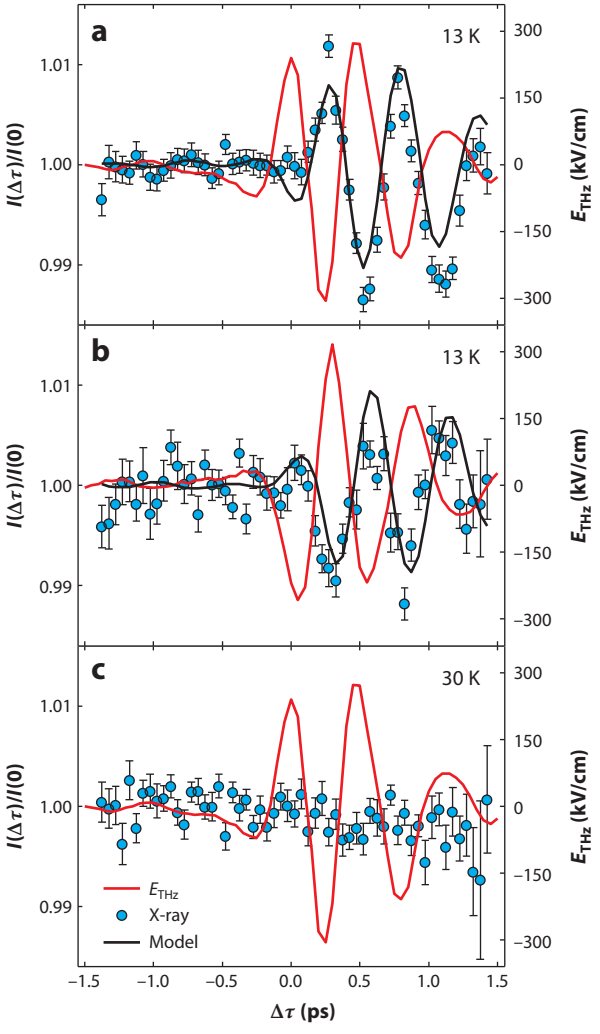

Figure 2

Measured coherent magnetic component of a coherent electromagnon in $TbMnO_3$ driven by THz radiation. (*a*,*b*) The red curve denotes driving THz field for two different phases of the driving field. The blue circles denote measured intensity from the resonant X-ray magnetic peak. The solid curve denotes results of a simple driven harmonic oscillator model of the dynamics. (*c*) Response of the system in the higher-temperature nonmultiferroic sinusoidal phase in which no electromagnon excitation is seen. Figure adapted with permission from Reference 71.

the intensity of the Bragg peaks through the Debye-Waller factor and give rise to diffuse scattering between the Bragg peaks. In equilibrium, the diffuse scattering due to phonons is related to the two-time density-density correlations $\langle Q_{\mathbf{k}s}(0)Q_{-\mathbf{k}s}(t)\rangle$ (73). Inelastic X-ray scattering measurements obtain the spectrum of excitations that is proportional to the Fourier transform of these correlations (the dynamical structure factor). Because the phonon frequencies are typically at least six orders of magnitude lower than the X-ray frequency, very high resolution monochromators and analyzers are required to measure the energy loss (or gain) that occurs in the inelastic scattering process (74, pp. 317–70; 75, pp. 1–68; 76, pp. 1–32). The high flux and short pulse duration of the

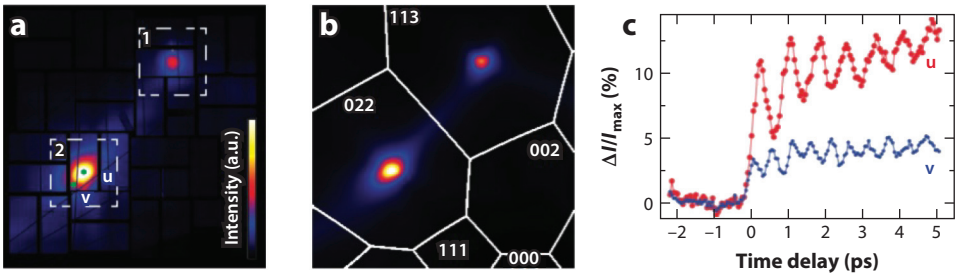

Figure 3

(*a*) Measured and (*b*) calculated thermal diffuse scattering from (001) Ge (unexcited) using 10-keV X-rays. (*c*) Change in the X-ray diffuse scattering as a function of time delay following photoexcitation with a 1.55-eV pump for the two points labeled u and v in panel *a*. Adapted with permission from Reference 72.

hard-X-ray FEL allow for the study of higher-order coherences directly in the time domain without high-resolution monochromators or analyzers, which offers important advantages for measuring low-energy collective modes both in and far from equilibrium (72) as well as with exquisite energy and momentum resolution (77).

The ability to generate and detect high-wave-vector phonons in the time domain was first demonstrated by Trigo et al. (72) in optical pump, femtosecond X-ray diffuse scattering probe experiments. The method, dubbed Fourier transform inelastic X-ray scattering (FT-IXS), used a short, 800-nm pump pulse to promote electrons from the valence band to the conduction band in a single crystal of Ge. Following the optical pump pulse, 10-keV X-rays from the LCLS FEL strike the sample at grazing incidence and are scattered in all directions. A multipixel array detector simultaneously captures a large collection angle, corresponding to scattering vectors lying in multiple Brillouin zones (see **Figure 3**). By analyzing the time dependence of the diffuse scattering as a function of momentum transfer, the authors were able to map out the transverse acoustic dispersion over a wide range of the Brillouin zone. The highest-frequency phonon that can be detected is limited both by the pump and probe durations and by uncertainty in the time delay. In the initial experiments, the timing jitter between the pump and probe pulses was a major factor limiting the experiment. Recent advances, including those in shot-by-shot timing described above, allow for measurements of the dispersion throughout the entire Brillouin zone (77). In both experiments, the results were interpreted in terms of thermal phonon squeezing and the generation of correlated phonon pairs of equal and opposite momenta that exhibit second-order temporal coherences. This interpretation was later validated in coherent control experiments in which an optical pulse pair was used to preferentially amplify or suppress the temporal coherences (46).

Electron-phonon interactions can generate such higher-order coherences, for example, through second-order Raman scattering processes that couple to a continuum of modes spanning the Brillouin zone. This allows high-wave-vector phonons to be excited by low-wave-vector optical excitation as long as they are produced in correlated pairs of near equal and opposite momentum. In the case of ultrafast excitation, squeezed modes are produced through transient changes in the mode frequencies. In this case, the equal-time displacement-displacement correlations, $g_{\mathbf{k}_S}(t) = \langle Q_{\mathbf{k}_S} Q_{-\mathbf{k}_S}(t) \rangle$, oscillate at twice the excited phonon frequencies, $g(t) \propto \cos(2\Omega_{q_S} t)$ (72). The oscillations in these second-order displacement correlations had previously been seen both in optical experiments through transient changes to the dielectric function (78) and in X-ray diffraction experiments as transient changes to the Debye-Waller factor (79). However, in both of these cases, the experimental observable includes a sum over a density of states such that they give

FT-IXS: Fourier transform inelastic X-ray scattering

indirect information about the average structure. In contrast, the ability to measure excitations with momentum and time resolution provides a significant advantage and can lead to measurements of excited state forces as well as to coupling between modes. As described below, the technique has recently been used to elucidate the nature of the ferroelectric instability in PbTe, which was due to electron-phonon interactions involving specific states near the direct band gap, similar to the Peierls mechanism (80). In that experiment, finite correlations were excited for phonons with equal and opposite momentum but belonging to different branches, leading to temporal oscillations in the diffuse scattering at the sum and difference frequencies (squeezed combination modes).

4. PHASE TRANSITIONS

The early experiments in the field of ultrafast X-ray scattering involved studies of solid-liquid or order-to-disorder transitions (8, 14, 81, 82), chosen in part due to the possibility of large-amplitude, optically driven changes in the diffracted X-ray intensity and stemming from earlier optical pump-probe studies (83, 84). One of the powerful results of ultrabright X-ray sources is the ability to probe potentially irreversible dynamics in a single-shot manner. This new capability enables probing of structural intermediates associated with energy barrier crossings during first-order phase transitions. Importantly, these atomistic studies enable some of the earliest direct comparisons with first-principles modeling of the initial steps in these transitions. We review here two recent examples along these lines, probing high-pressure/shock-induced transformations. In the first example, measurements by Milathianaki et al. (85) probed the atomistic response of a prototypical metal, Cu, to transient shocks of amplitude 70 GPa. Whereas previous studies probed these dynamical responses on nanosecond timescales (86), this was one of the first studies to probe the first primary steps in a shock-induced phase transition, in this case, probing the transition from uniaxial elastic compression to three-dimensional plastic flow and enabling direct comparison to multimillion-atom molecular dynamics simulations. Here an optical laser launched the shock through an ablation-driven process in which material ablated from the surface launches a corresponding compression wave by momentum conservation into the solid. The dynamics were probed by femtosecond X-rays at the LCLS in a transmission geometry, recording changes in the radius of the associated Debye-Scherrer diffraction rings as a direct measure of the lattice strain (**Figure 4**), with diffraction rings arising from an ensemble of quasi-randomly oriented crystallites. In particular, it was possible to distinguish and separate the elastic and plastic responses of the material by making use of the fact that, for a uniaxial shock propagating in the direction perpendicular to the sample surface, X-ray reflections with small Bragg angle correspond to lattice planes almost parallel to the shock direction, thereby reducing the magnitude of the observed strain response. In contrast, under conditions in which the large pressures drive a transition to a plastic, more hydrostatic pressure, the stress is felt from all directions, and the magnitude of the measured lattice strain is enhanced. In this way, a kind of tomography of the lattice response can be carried out by probing many reflections, with the magnitude of the observed diffraction peak shifts scaling like $\sin^2 \theta_B$ (87), where θ_B is the Bragg angle. Similar effects have been observed that are associated with breathing mode responses in nanocrystals (88), for which well-defined radial breathing modes in CdS nanowires lead to a similar $\sin^2 \Psi_{bkl}$ dependence of the magnitude of the shift in the corresponding Bragg peaks, where Ψ_{bkl} is the angle that a particular reciprocal lattice vector with Miller indices (bkl) makes with respect to the radial direction of the nanorod.

In our second example, related measurements at the LCLS (using the same ablation-driven shock generation technique) were carried out, probing picosecond-shock-driven phase transitions in nanocrystals (89). These studies were motivated by attempts to understand the

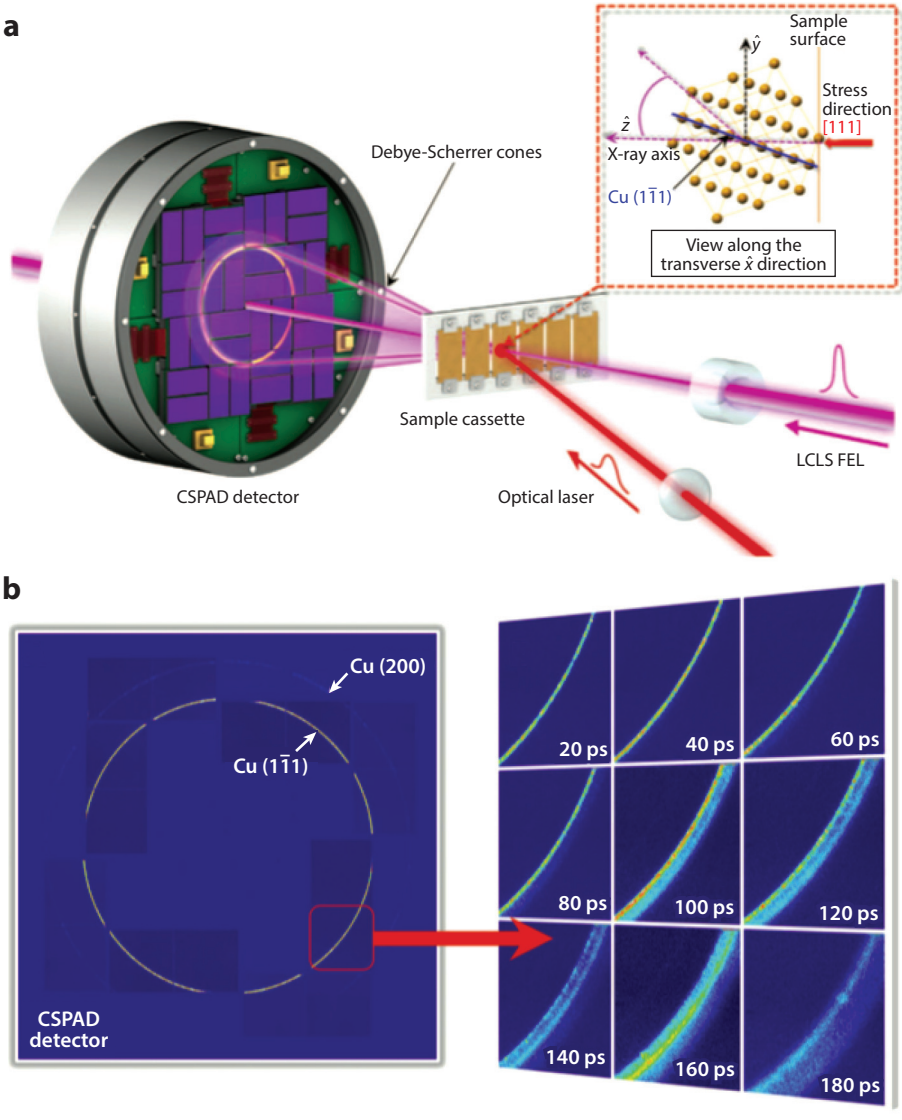

Figure 4

Experimental setup and raw data showing shock compression of Cu. (*a*) Experimental setup showing a single-shot pump-probe scheme. An optical pulse launches a high-pressure shock into a bulk solid with the lattice response probed in transmission by femtosecond X-ray pulses. (*b*) Raw data showing a shift of the Debye-Scherrer diffraction rings to higher-momentum transfer (Q) on picosecond timescales and a transition from elastic strain to plastic strain. Abbreviations: CSPAD, Cornell-SLAC Pixel Array Detector; FEL, free-electron laser; LCLS, Linac Coherent Light Source. Adapted with permission from Reference 85.

intermediate states and dynamical pathways that materials follow during first-order pressure-induced phase transitions. Nanocrystals represent model systems for this kind of study because they behave as individual crystalline domains and separate the competing processes of nucleation and growth (90). Whereas the kinetics of these processes had been studied in detail in nanocrystalline systems (91, 92), the associated dynamics and atomic-scale pathways associated with this

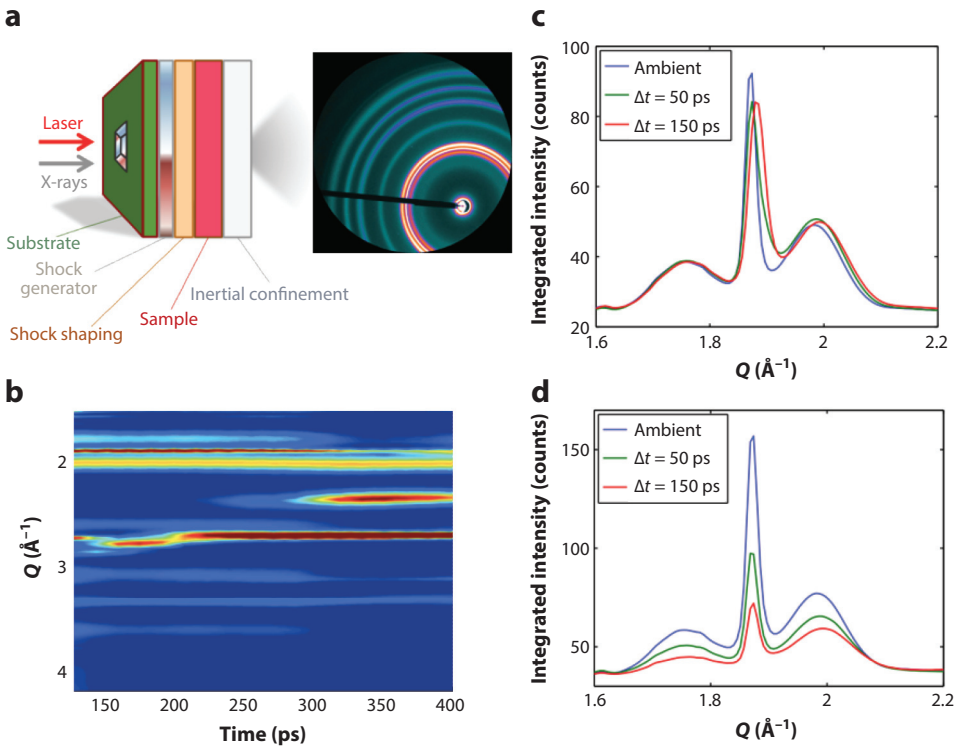

Figure 5

(*a*) Schematic for laser-driven shock studies of CdS nanorods and the resulting transmission diffraction pattern. (*b*) Diffractogram showing the time-resolved X-ray diffraction response as a function of time and momentum transfer (*Q*). The phase transition from the low-pressure wurtzite phase to the high-pressure rocksalt phase is manifested by the appearance of the (200) Bragg peak, which is forbidden in the low-pressure phase. (*c*) Analysis of the (002) dynamic response showing evidence at low stress for predicted initial compression along the *c*-axis. (*d*) At high pressures, a different transformation pathway emerges. Adapted with permission from Reference 89.

transition were not understood. **Figure 5** shows the result of an ensemble of single-shot measurements in which a picosecond-rise-time shock with amplitude ≈10 GPa drives the system from a wurtzite phase at equilibrium into a metastable rocksalt phase at high pressure. This process is manifested most obviously by the appearance of a previously symmetry-forbidden (200) reflection that grows in at $Q \approx 2.3$ Å^{-1}. However, more information can be obtained by probing time-dependent shifts in the Bragg peaks and comparing the results with first-principles simulations. In particular, prior theoretical studies had predicted that the transformation pathway for these systems involved an initial compression along the *c*-axis of the nanorod to form a five-coordinate h-MgO-type intermediate followed by compressive shear along the *a*-axis toward the cubic rocksalt structure (93, 94). The measurements show that, just below the transformation threshold, the structure indeed approaches the five-coordinate h-MgO-type intermediate observed under simulated hydrostatic compression, showing the dominant compression along the *c*-axis that is associated with a shift of the (002) reflection to higher *Q* (**Figure 5**). In contrast, the orthogonal (100) reflection does not shift, and the intermediate (101) shifts a smaller amount, as would be expected. However, when brought above the transformation threshold by shock compression,

the h-MgO structure is not observed. Instead, the wurtzite (002) reflection simply decreases as the rocksalt (200) grows in, without evidence for any shift in the (002) reflection as observed at lower pressures. The decreasing prevalence of the intermediate with increasing shock stress indicates that a different pathway for the transformation becomes possible at high shock stresses, in close analogy with the action of a catalyst in a chemical reaction. More recently, studies of phase transitions at the nanoscale have been carried out at the single-nanoparticle level, making use of the transverse coherence of X-ray FELs at the LCLS and at SACLA (95–97). These studies are discussed in further detail below.

In addition to the strongly first-order transitions discussed above, recent efforts have been able to significantly extend these studies toward the study of phase transitions in strongly correlated materials, involving contributions from charge, orbital, and structural degrees of freedom. In an experiment on the charge-ordered phase of the perovskite manganite $Pr_{0.5}Ca_{0.5}MnO_3$, Beaud et al. (98) applied time-resolved X-ray scattering to study the interplay between charge order, orbital order, and structure during a phase transition induced by strong near-infrared absorption with a 55-fs-duration light pulse. In this experiment, the X-ray energy was tuned to the vicinity of the Mn K-edge, which strongly enhances second-order scattering contributions from valence states of the Mn ions that are normally too weak to be detected. This energy tuning allowed for selective probing of different types of long-range order in the system, as shown in **Figure 6**. The $(0\bar{3}0)$ peak is sensitive primarily to the valence charge ordering on the Mn ions. The intensity of diffraction from this peak is suppressed on a timescale of approximately 100 fs, limited by the time resolution of the experiment. Above 5 mJ/cm^2 fluence, the excitation from the laser completely suppresses the diffraction from this peak, implying that the charge order is completely melted on this timescale. The other two diffraction peaks shown are sensitive either to the purely structural superlattice distortion [the $(\bar{2}\,\frac{1}{2}\,0)$ peak] or to a combination of orbital order and local Jahn-Teller distortions [the $(0\,\frac{\bar{5}}{2}\,0)$ peak]. The dynamics of the intensity for these diffraction peaks show oscillatory dynamics that persist after the melting of charge order, suggesting that these orders are not directly melted by the excitation process but are instead coupled to the melting of charge order. A model of this coupling treating the melting process as driven by a single time-dependent order parameter that is coupled to each of these different types of order

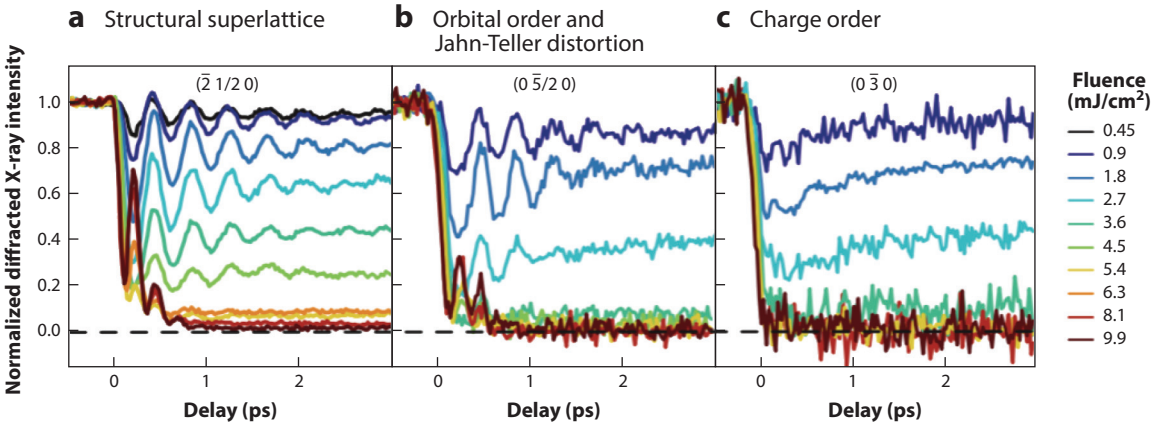

Figure 6

Measured light-induced changes in X-ray scattering in $Pr_{0.5}Ca_{0.5}MnO_3$ near the Mn K-edge for three superlattice reflections sensitive to (*a*) structural, (*b*) orbital, and (*c*) charge order. Measurements show that light excitation melts the Mn valence order before coupling to the orbital and structural degrees of freedom. Adapted with permission from Reference 98.

successfully explained the main features of the dynamics connected with the phase transition, which includes large-amplitude coherent oscillations of the structure in the transiently created molten phase.

5. ELECTRONIC/CHARGE-DRIVEN PROCESSES

The functionality of materials is often determined by energy exchange between electronic and lattice degrees of freedom, and femtosecond X-ray scattering studies provide a unique window into these processes. For example, the efficiency of a solar cell is determined in part by hot carrier relaxation following photon absorption; X-ray studies sensitive to lattice motion can capture the first steps in how the lattice heats up, as reflected in the increased RMS displacements of the atoms in a crystal (8, 99, 100), in this way directly resolving in the time domain the flow of energy between these different degrees of freedom. In many cases, as noted above, carrier excitation can lead to nonthermal excitations, e.g., electron-phonon coupling processes in which electronic excitation directly leads to a carrier-driven stress. The study on $Pr_{0.5}Ca_{0.5}MnO_3$ discussed above represents a good example of such an effect. The first investigations of carrier-driven structural deformations were carried out by optical pump-probe experiments that indirectly probed the carrier-induced stress on picosecond timescales, as reflected in changes to macroscopic properties such as the index of refraction (38, 84), but recent studies have been able to probe these unique lattice responses directly in the time domain at atomic resolution (41, 82, 88, 101, 102).

In materials that exhibit strong coupling between electronic and lattice degrees of freedom, these effects can be particularly important. For example, in ferroelectric materials, the intrinsic polarization, which underlies their key functionality with respect to information storage technologies, is strongly coupled to electronic degrees of freedom, including currents and surface charges. In one interesting example, consider that one may switch the polarization in a thin film ferroelectric by modulating the oxygen partial pressure above the surface, an effect driven by charge compensation that modulates the depolarization field in a ferroelectric (104, 105). These depolarization fields can be compensated for by the presence of electrodes (106, 107) or by free carriers, opening up new means for all-optically manipulating the functional properties of such materials. For example, optical excitation leads to the development of time-dependent currents, e.g., a bulk photovoltaic effect (108–110), which in turn can couple to structural degrees of freedom, representing a kind of all-optical bias. Recent femtosecond X-ray scattering studies have investigated these processes at the LCLS, probing optically driven structural changes in $PbTiO_3$ thin films (103). Measurements probed time-dependent shifts in the out-of-plane (003) reflection following above-gap 400-nm excitation. At room temperature, the film stabilizes in a monodomain phase, with polarization normal to the film (111). In contrast to the response observed under simple thermal heating effects (e.g., a contraction of the *c*-axis lattice parameter associated with a reduction in the tetragonality of the unit cell), the observed dynamics exhibit a significantly more complex response (see **Figure 7**). In particular, a short-time compressive response is observed, followed by a long-lived expansive effect, which saturates as a function of fluence (not shown in **Figure 7**). At higher temperatures, the volatile adsorbates that stabilize the monodomain phase are removed, and a stripe phase is formed that consists of alternating regions of opposite polarization with period of order 10 nm. This phase transition is driven under static conditions by a trade-off between the energy of the uncompensated depolarization field and the domain walls. Under these initial conditions, a similar dynamical response in the *c*-axis dynamics is observed following photon absorption. In addition, dynamic changes in the satellites associated with the stripe phase are seen; in particular, there is a long-lived increase in the domain period, as reflected in changes in the radius of this diffuse side band. Taken together, all these effects are consistent with an optically

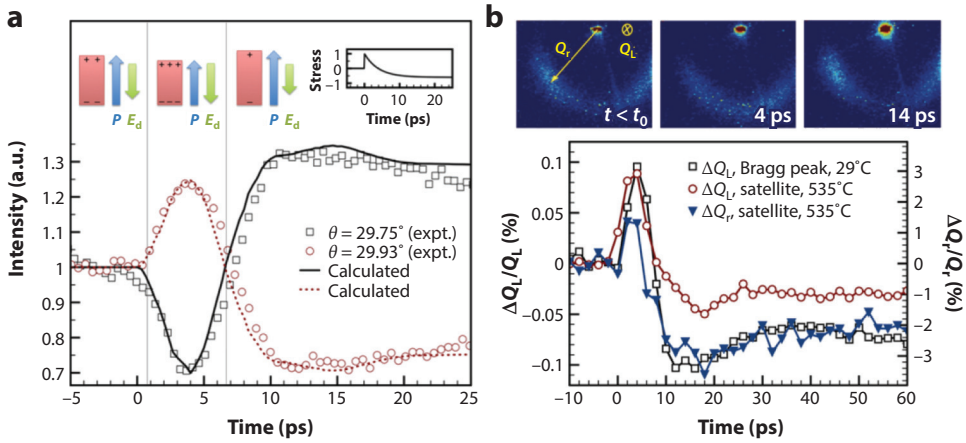

Figure 7

(*a*) Time-dependent changes in the (003) reflection from a $PbTiO_3$ thin film on a $SrTiO_3$ substrate measured on the left and right sides of rocking curve peak (*squares* and *circles*, respectively). Following a short-time compressive feature associated with a transient photo-induced shift current response, a long-lived expansive response is observed, occurring in the opposite direction as that expected for a simple temperature jump. This expansion is associated with a carrier-driven screening of the depolarization field that leads to increased tetragonality as measured. Solid lines are fits using the time-dependent stress shown in the inset. (*b*) Transient changes in diffuse scattering associated with ferroelectric stripe phase observed at higher static temperature (535°C). These changes are characterized by domains of opposite polarization with period of order 10 nm. The figure shows both extracted time-dependent changes in the out-of-plane *c*-axis, consistent with those measured at room temperature, and changes in the stripe domain period, consistent with an ultrafast screening of the depolarization field. Adapted with permission from Reference 103.

driven screening of the depolarization field through carrier excitation. Recent studies in related ferroelectric and multiferroic systems have confirmed the above interpretations (16, 112). In contrast to the above measurements, in which carrier excitation modulated the internal electric fields within a ferroelectric thin film, related measurements have directly probed the influence of ultrafast electric fields on $BaTiO_3$ ferroelectric thin films in a THz pump–X-ray probe geometry (113). In these studies, a THz pump pulse acts as an ultrafast electric field bias oriented perpendicular to the out-of-plane ferroelectric polarization. Modulations in the (003) structure factor indicated large-amplitude rotations of the polarization in addition to lattice strains associated with resonant excitation of the ferroelectric soft mode.

A related example concerns time domain studies of PbTe, a narrow-gap semiconductor and high-temperature thermoelectric material that exhibits incipient ferroelectric behavior. It shares many similarities with other group IV–VI and V and related materials that exhibit coupled electronic and lattice instabilities (114, 115). Here small differences in the microscopic properties can lead to large changes in the macroscopic properties. The thermoelectric behavior of PbTe has been linked to large anharmonic interactions and to its incipient ferroelectricity (116). In addition, inelastic neutron scattering results show large anomalies in the soft transverse optical mode that has been interpreted in terms of both extended anharmonic interactions between modes (117) and local symmetry breaking (118). Motivated by these studies, Jiang et al. (80) used femtosecond X-ray diffuse scattering to investigate the nature of the ferroelectric instability. By using ultrafast optical excitation just above the direct band gap, they produced a nonequilibrium population of electrons and holes in the very states at the band edges that are expected to play an important role in determining the equilibrium structure. Importantly, the ultrafast electronic excitation triggers

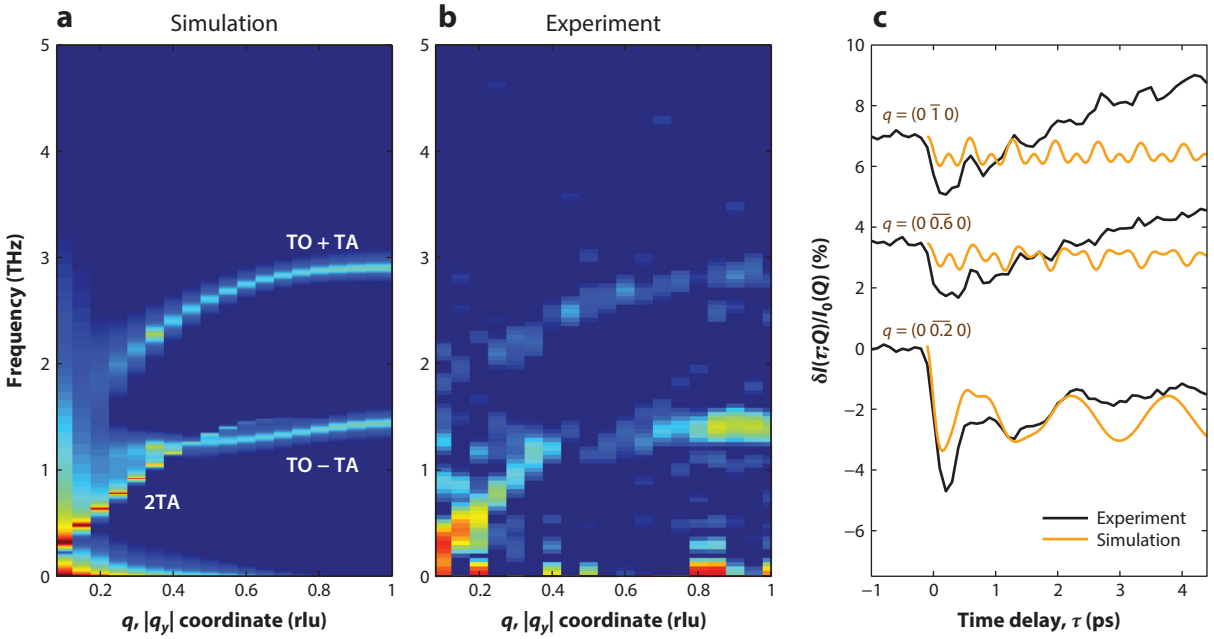

Figure 8

(*a*) Simulation and (*b*) experimental FT-IXS spectra for PbTe photoexcited with 2-μm radiation, measured along the Δ line in the ($\bar{1}$13) Brillouin zone. The data show overtone and combination modes at 2TA and TO ± TA frequencies that are consistent with photoexcitation weakening the ferroelectric instability and further stabilizing the paraelectric state. TA denotes transverse acoustic, and TO denotes transverse optical. (*c*) Comparison of time-dependent scattering for both simulation and experiment at select wave vectors. The simulation does not include the picosecond-timescale heating of the lattice. Reproduced with permission from Reference 80.

a transformation to such a state at constant volume and without introducing the defects associated with chemical doping. Some results for the FT-IXS spectra are shown in **Figure 8**, which also includes simulations based on first-principles calculations for both the ground and excited states. Unlike previous FT-IXS results on Ge (72, 77), the data show both overtones and combination modes. The latter results from a differential change in the real-space force constants and is consistent with previous studies showing that long-range interactions are due to the resonant bonding of the unsaturated *p* orbitals (119). In this case, photoexcitation further stabilizes the paraelectric state, renormalizing the phonon modes, including hardening the soft TO mode near the zone center, softening the modes near the zone edge, and changing the eigenvectors causing a mixing of the acoustic and optic branches. The results are consistent with a Peierls-like instability, connecting the bond and band pictures of the ferroelectric distortion (114). Importantly, these findings show that electron-phonon interactions drive instability in a classic ferroelectric fashion and that the strong lattice anharmonicity is more a consequence than the driver of this behavior.

6. OUTLOOK

We conclude by briefly providing an outlook on the field of ultrafast X-ray scattering and where it may lead in the future, in particular making some further comments regarding single-particle studies. From a general perspective, femtosecond coherent X-ray sources provide a powerful means for visualizing atomic-scale processes as they evolve. However, all the studies described above were performed on bulk materials, thin films, or collections of nanoparticles and thus represent

ensemble averages. Heterogeneity is particularly important in determining materials properties. Therefore, extending such techniques with real-space imaging would be particularly valuable. Recent FEL experiments have made use of the high brightness to explore the dynamics of individual nanoparticles (see, e.g., References 95, 97, 120, 121). This approach could ultimately allow one to obtain critical information on how functionality varies with small changes in particle size, morphology, strain, defect concentrations, or surface preparation. For example, Bragg coherent diffraction imaging (BCDI) enables atomic-scale imaging of single particles, allowing for the detection of single dislocations and other defects by using iterative phase retrieval methods (122–124). Clark et al. (95) used this approach to generate real-space images of the generation and evolution of coherent acoustic phonons in a single gold nanocrystal through a combination of BCDI with pump-probe techniques. In this experiment, gold nanoparticles were excited by a femtosecond Ti:sapphire laser, and their individual coherent diffraction patterns were tracked in time. The angular position of the Bragg peaks showed oscillations on the picosecond timescale that correspond to two vibrational breathing modes of the nanocrystal. However, because BCDI retrieves the amplitude and phase of a Bragg peak, Clark et al. were able to extract much more information, generating three-dimensional dynamical strain maps with picometer sensitivity and nanometer spatial resolution, as shown in **Figure 9**. They were thus able to detect coherent shear modes that would otherwise have been undetectable from the position of the Bragg peak. In a later experiment, Clark et al. (97) used the same technique to image transient but fully reversible melting and acoustic mode softening in gold nanoparticles, consistent with a core-shell model for melting. Similarly, measurements at SACLA applied coherent imaging techniques to probe phase transition dynamics in single VO_2 nanocrystals (120). Finally, Ferguson et al. (121) used an X-ray pump–X-ray probe technique using two 10-fs X-ray pulses at ≈8.3 keV with adjustable delay (associated with the radiation from two independent electron bunches within the undulator with slightly different energies) to probe X-ray–induced lattice changes in a single 70-nm xenon van der Waals cluster. A first intense X-ray pulse focused to an ≈100-nm spot size ionized the cluster, and the second pulse probed the induced structural changes in the single particle through changes in the position of the Bragg peak as measured on a large-area detector (**Figure 9**). Surprisingly, a short-time collective compression effect was observed to develop on a timescale of tens of

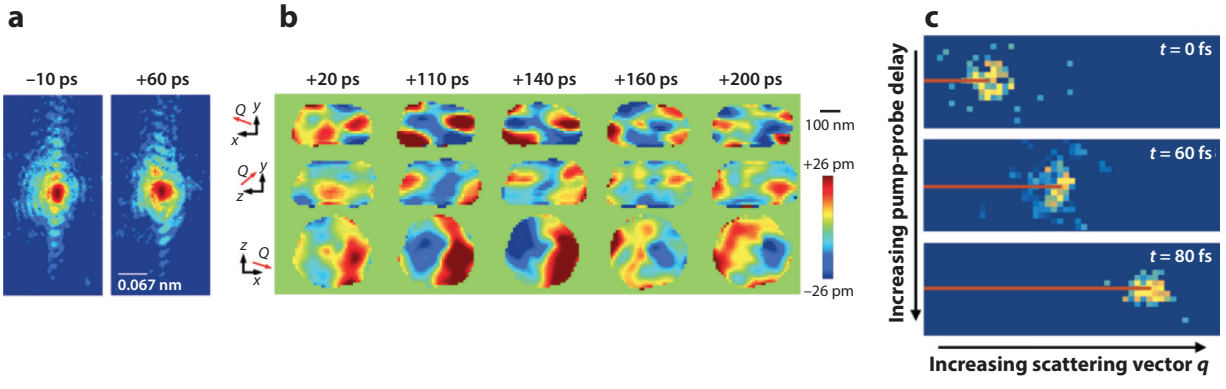

Figure 9

(*a*) Raw coherent diffraction snapshots from single gold nanocrystals at two different time delays following photoexcitation. (*b*) Reconstructed real-space image of the evolution of coherent acoustic phonons within a nanocrystal. (*c*) Raw data from X-ray pump–X-ray probe studies of the structural response of a single xenon cluster, showing X-ray–induced lattice contractions associated with a shift of the Bragg peaks to higher *Q*. Adapted with permission from References 95 and 121.

femtoseconds, which the authors explained via an electron delocalization effect associated with the X-ray–induced solid-to-plasma transition. The high flux of the FEL allows for X-ray pump–X-ray probe studies more generally, as was recently demonstrated in Reference 125, in which the authors used the SACLA FEL to visualize X-ray–induced atomic displacements in diamond. These studies are important for understanding the limitations of single-particle X-ray imaging.

The experiments described above provide an early glimpse at the potential for probing the dynamics of single nanosized materials or within spatially heterogeneous systems with variation or disorder at the nanoscale. Multiple-pulse X-ray studies associated with X-ray photon correlation spectroscopy techniques have the potential to further extend these measurements to probe not just equilibrium fluctuation dynamics (126, 127) but also the structural fluctuations that occur during nonequilibrium events, e.g., dynamics in the presence of an energy barrier, as often occurs during first-order phase transformations. Significantly, many of the experiments discussed above will benefit from next-generation FEL sources projected to turn on in the very near future, enabling high-repetition-rate (MHz) studies of materials dynamics (128). Here challenges await as well with respect to sample reversibility, but there are already experiments that demonstrate the feasibility of such approaches (21–23). Finally, new source developments are pushing toward even shorter wavelengths, enabling higher-resolution dynamical snapshots and the application of pair distribution function techniques (129) to resolve atomic-scale motions.

SUMMARY POINTS

1. In the last five years, new opportunities have emerged, enabled by the development of X-ray free-electron lasers, which dramatically enhance our ability to probe atomic-scale rearrangements in real time on femtosecond timescales in situ.
2. Applications of these new sources extend beyond the realm of materials science to, for example, biology, chemistry, physics, and geophysics.
3. With respect to materials science, these techniques provide a new means for visualizing materials functionality and the flow of energy between different degrees of freedom in complex materials and devices, under both near-equilibrium and highly nonequilibrium/single-shot conditions.
4. These visualization techniques in turn couple directly to first-principles modeling and simulations.

FUTURE ISSUES

1. The use of the transverse coherence of X-ray free-electron laser beams for dynamic coherent imaging of structure is still in its early stages. Early demonstration experiments show the power of this approach to visualize in three dimensions the dynamics of nanocrystalline or spatially heterogeneous systems, but novel opportunities remain.
2. New opportunities at higher repetition rates are emerging, extending current studies at 120 Hz by several orders of magnitude. The range of materials systems that can be explored through these new sources will expand even further, in particular toward studies in the near-equilibrium limit with sensitivity to the lattice deformations that occur in near-equilibrium conditions.

DISCLOSURE STATEMENT

The authors are not aware of any affiliations, memberships, funding, or financial holdings that might be perceived as affecting the objectivity of this review.

ACKNOWLEDGMENTS

A.M.L. and D.A.R. acknowledge support from the Materials Science and Engineering Division, Office of Science, US Department of Energy. S.L.J. acknowledges support from the NCCR MUST, funded by the Swiss National Science Foundation. Use of the LCLS at SLAC National Accelerator Laboratory is supported by the US Office of Basic Energy Sciences, Office of Science, US Department of Energy, under contract DE-AC02-76SF00515.

LITERATURE CITED

1. Barends TRM, Foucar L, Ardevol A, Nass K, Aquila A, et al. 2015. Direct observation of ultrafast collective motions in CO myoglobin upon ligand dissociation. *Science* 350:445–50
2. Sokolowski-Tinten K, Blome C, Blums J, Cavalleri A, Dietrich C, et al. 2003. Femtosecond X-ray measurement of coherent lattice vibrations near the Lindemann stability limit. *Nature* 422:287–89
3. Fritz DM, Reis DA, Adams B, Akre RA, Arthur J, et al. 2007. Ultrafast bond softening in bismuth: mapping a solid's interatomic potential with X-rays. *Science* 316:633–36
4. Bostedt C, Boutet S, Fritz DM, Huang Z, Lee HJ, et al. 2016. Linac Coherent Light Source: the first five years. *Rev. Mod. Phys.* 88:015007
5. Cavalieri AL, Fritz DM, Lee SH, Bucksbaum PH, Reis DA, et al. 2005. Clocking femtosecond X-rays. *Phys. Rev. Lett.* 94:114801
6. Harmand M, Coffee R, Bionta M, Chollet M, French D, et al. 2013. Achieving few-femtosecond time-sorting at hard X-ray free-electron lasers. *Nat. Photon.* 7:215–218
7. Bionta MR, Hartmann N, Weaver M, French D, Nicholson DJ, et al. 2014. Spectral encoding method for measuring the relative arrival time between X-ray/optical pulses. *Rev. Sci. Instrum.* 85:083116
8. Lindenberg AM, Larsson J, Sokolowski-Tinten K, Gaffney KJ, Blome C, et al. 2005. Atomic-scale visualization of inertial dynamics. *Science* 308:392–95
9. Neutze R, Hajdu J. 1997. Femtosecond time resolution in X-ray diffraction experiments. *PNAS* 94:5651–55
10. Reis D, Lindenberg A. 2007. *Ultrafast X-Ray Scattering in Solids*. Berlin/Heidelberg: Springer
11. Murnane MM, Kapteyn HC. 1991. Ultrafast X-ray pulses from laser-produced plasmas. *Science* 251:531–36
12. Rousse A, Audebert P, Geindre JP, Falliès F, Gauthier JC, et al. 1994. Efficient K_α X-ray source from femtosecond laser-produced plasmas. *Phys. Rev. E* 50:2200–7
13. von der Linde D, Sokolowski-Tinten K, Blome C, Dietrich C, Tarasevitch A, et al. 2001. 'Ultrafast' extended to X-rays: femtosecond time-resolved X-ray diffraction. *Z. Phys. Chem.* 215:1527–41
14. Siders CW, Cavalleri A, Sokolowski-Tinten K, Tóth C, Guo T, et al. 1999. Detection of nonthermal melting by ultrafast X-ray diffraction. *Science* 286:1340–42
15. Weisshaupt J, Juvé V, Holtz M, Ku S, Woerner M, et al. 2014. High-brightness table-top hard X-ray source driven by sub-100-femtosecond mid-infrared pulses. *Nat. Photon.* 8:927–30
16. Schick D, Herzog M, Wen H, Chen P, Adamo C, et al. 2014. Localized excited charge carriers generate ultrafast inhomogeneous strain in the multiferroic $BiFeO_3$. *Phys. Rev. Lett.* 112:097602
17. Chang Z, Rundquist A, Zhou J, Murnane MM. 1996. Demonstration of a subpicosecond X-ray streak camera. *Appl. Phys. Lett.* 69:133–35
18. Larsson J, Heimann P, Lindenberg A, Schuck P, Bucksbaum P, et al. 1998. Ultrafast structural changes measured by time-resolved X-ray diffraction. *Appl. Phys. A* 66:587–91
19. Lindenberg AM, Kang I, Johnson SL, Missalla T, et al. 2000. Time-resolved X-ray diffraction from coherent phonons during a laser-induced phase transition. *Phys. Rev. Lett.* 84:111–14

20. DeCamp MF, Reis DA, Cavalieri A, Bucksbaum PH, Clarke R, et al. 2003. Transient strain driven by a dense electron-hole plasma. *Phys. Rev. Lett.* 91:165502
21. Kozina M, Hu T, Wittenberg J, Szilagyi E, Trigo M, et al. 2014. Measurement of transient atomic displacements in thin films with picosecond and femtometer resolution. *Struct. Dyn.* 1:034301
22. Navirian H, Shayduk R, Leitenberger W, Goldshteyn J, Gaal P, Bargheer M. 2012. Synchrotron-based ultrafast X-ray diffraction at high repetition rates. *Rev. Sci. Instrum.* 83:063303
23. March AM, Stickrath A, Doumy G, Kanter EP, Krässig B, et al. 2011. Development of high-repetition-rate laser pump/X-ray probe methodologies for synchrotron facilities. *Rev. Sci. Instrum.* 82:073110
24. Zholents A, Zolotorev M. 1996. Femtosecond X-ray pulses of synchrotron radiation. *Phys. Rev. Lett.* 76:912–15
25. Schoenlein RW, Chattopadhyay S, Chong HHW, Glover TE, Heimann PA, et al. 2000. Generation of femtosecond pulses of synchrotron radiation. *Science* 287:2237–40
26. Khan S, Holldack K, Kachel T, Mitzner R, Quast T. 2006. Femtosecond undulator radiation from sliced electron bunches. *Phys. Rev. Lett.* 97:074801
27. Beaud P, Johnson SL, Streun A, Abela R, Abramsohn D, et al. 2007. Spatiotemporal stability of a femtosecond hard-X-ray undulator source studied by control of coherent optical phonons. *Phys. Rev. Lett.* 99:174801
28. Issenmann D, Ibrahimkutty S, Steininger R, Göttlicher J, Baumbach T, et al. 2013. Ultrafast laser pump X-ray probe experiments by means of asynchronous sampling. *J. Phys. Conf. Ser.* 425:092007
29. Laulhé C, Cammarata M, Servol M, Miller RJD, Hada M, Ravy S. 2013. Impact of laser on bismuth thin-films. *Eur. Phys. J. Spec. Top.* 222:1277–85
30. Huang X, Safranek J, Corbett J, Nosochkov Y, Sebek J, Terebilo A. 2007. Low alpha mode for SPEAR3. In *2007 IEEE Particle Accelerator Conference (PAC)*, June 25–29
31. Fritz DM, Reis DA, Adams B, Akre R, Arthur J, et al. 2007. Ultrafast bond softening in bismuth: mapping a solid's interatomic potential with X-rays. *Science* 315:633–36
32. Emma P, Akre R, Arthur J, Bionta R, Bostedt C, et al. 2010. First lasing and operation of an angstrom-wavelength free-electron laser. *Nat. Photon.* 4:641–47
33. Ishikawa T, Aoyagi H, Asaka T, Asano Y, Azumi N, et al. 2012. A compact X-ray free-electron laser emitting in the sub-ångström region. *Nat. Photon.* 6:540–44
34. Altarelli M. 2015. The European X-Ray Free-Electron Laser: toward an ultra-bright, high repetition-rate X-ray source. *High Power Laser Sci. Eng.* 3:e18
35. Ko IS, Han JH. 2014. Current status of PAL-XFEL. In *Proc. LINAC2014*, Geneva
36. Patterson BD, Beaud P, Braun HH, Dejoiea C, Ingold G, et al. 2014. Science opportunities at the SwissFEL X-ray laser. *Chimia* 68:73–78
37. Glauber R. 1963. Coherent and incoherent states of the radiation field. *Phys. Rev.* 131:2766–88
38. Thomsen C, Grahn H, Maris H, Tauc J. 1986. Surface generation and detection of phonons by picosecond light pulses. *Phys. Rev. B* 34:4129–38
39. Rose-Petruck C, Jimenez R, Guo T, Cavalleri A, Siders CW, et al. 1999. Picosecond–milliångström lattice dynamics measured by ultrafast X-ray diffraction. *Nature* 398:310–12
40. Reis DA, DeCamp M, Bucksbaum P, Clarke R, Dufresne E, et al. 2001. Probing impulsive strain propagation with X-ray pulses. *Phys. Rev. Lett.* 86:3072–75
41. Henighan T, Trigo M, Bonetti S, Granitzka P, Higley D, et al. 2016. Generation mechanism of terahertz coherent acoustic phonons in Fe. *Phys. Rev. B* 93:220301
42. Chen J, Tomov IV, Elsayed-Ali HE. 2006. Hot electrons blast wave generated by femtosecond laser pulses on thin Au(111) crystal, monitored by subpicosecond X-ray diffraction. *Chem. Phys. Lett.* 419:374–78
43. Zeiger HJ, Vidal J, Cheng TK, Ippen EP, Dresselhaus G, Dresselhaus MS. 1992. Theory for displacive excitation of coherent phonons. *Phys. Rev. B* 45:768–78
44. Kuznetsov AV, Stanton CJ. 1994. Theory of coherent phonon oscillations in semiconductors. *Phys. Rev. Lett.* 73:3243–46
45. Merlin R. 1997. Generating coherent THz phonons with light pulses. *Solid State Commun.* 102:207–20
46. Henighan T, Trigo M, Chollet M, Clark JN, Fahy S, et al. 2016. Control of two-phonon correlations and the mechanism of high-wavevector phonon generation by ultrafast light pulses. *Phys. Rev. B* 94:020302

47. Carles R, Zwick A, Renucci M, Renucci J. 1982. A new experimental method for the determination of the one phonon density of states in GaAs. *Solid State Commun.* 41:557–60
48. Johnson SL, Vorobeva E, Beaud P, Milne CJ, Ingold G. 2009. Full reconstruction of a crystal unit cell structure during coherent femtosecond motion. *Phys. Rev. Lett.* 103:205501
49. Johnson SL, Beaud P, Milne CJ, Krasniqi FS, Zijlstra ES, et al. 2008. Nanoscale depth-resolved coherent femtosecond motion in laser-excited bismuth. *Phys. Rev. Lett.* 100:155501
50. Johnson SL, Beaud P, Möhr-Vorobeva E, Caviezel A, Ingold G, Milne CJ. 2013. Direct observation of non-fully-symmetric coherent optical phonons by femtosecond X-ray diffraction. *Phys. Rev. B* 87:054301
51. Li JJ, Chen J, Reis DA, Fahy S, Merlin R. 2013. Optical probing of ultrafast electronic decay in Bi and Sb with slow phonons. *Phys. Rev. Lett.* 110:047401
52. Huang K. 1951. Lattice vibrations and optical waves in ionic crystals. *Nature* 167:779–80
53. Forst M, Manzoni C, Kaiser S, Tomioka Y, Tokura Y, et al. 2011. Nonlinear phononics as an ultrafast route to lattice control. *Nat. Phys.* 7:854–56
54. Mankowsky R, Först M, Cavalleri A. 2016. Non-equilibrium control of complex solids by nonlinear phononics. *Rep. Prog. Phys.* 79:064503
55. Subedi A, Cavalleri A, Georges A. 2014. Theory of nonlinear phononics for coherent light control of solids. *Phys. Rev. B* 89:220301(R)
56. Wallis R, Maradudin A. 1971. Ionic Raman effect. II. The first-order ionic Raman effect. *Phys. Rev. B* 3:2063
57. Martin T, Genzel L. 1974. Ionic Raman scattering and ionic frequency mixing. *Phys. Status Solid. B* 61:493–502
58. Hu W, Kaiser S, Nicoletti D, Hunt CR, Gierz I, et al. 2014. Optically enhanced coherent transport in $YBa_2Cu_3O_{6.5}$ by ultrafast redistribution of interlayer coupling. *Nat. Mater.* 13:705–11
59. Nicoletti D, Casandruc E, Laplace Y, Khanna V, Hunt CR, et al. 2014. Optically induced superconductivity in striped $La_{2-x}Ba_xCuO_4$ by polarization-selective excitation in the near infrared. *Phys. Rev. B* 90:100503
60. Kaiser S, Hunt CR, Nicoletti D, Hu W, Gierz I, et al. 2014. Optically induced coherent transport far above t_c in underdoped $YBa_2Cu_3O_{6+\delta}$. *Phys. Rev. B* 89:184516
61. Fausti D, Tobey RI, Dean N, Kaiser S, Dienst A, et al. 2011. Light-induced superconductivity in a stripe-ordered cuprate. *Science* 331:189–91
62. Mitrano M, Cantaluppi A, Nicoletti D, Kaiser S, Perucchi A, et al. 2016. Possible light-induced superconductivity in K_3C_{60} at high temperature. *Nature* 530:461–64
63. Mankowsky R, Subedi A, Forst M, Mariager SO, Chollet M, et al. 2014. Nonlinear lattice dynamics as a basis for enhanced superconductivity in $YBa_2Cu_3O_{6.5}$. *Nature* 516:71–73
64. Pimenov A, Mukhin AA, Ivanov VY, Travkin VD, Balbashov AM, Loidl A. 2006. Possible evidence for electromagnons in multiferroic manganites. *Nat. Phys.* 2:97–100
65. Kimura T, Goto T, Shintani H, Ishizaka K, Arima T, Tokura Y. 2003. Magnetic control of ferroelectric polarization. *Nature* 426:55–58
66. Kenzelmann M, Harris AB, Jonas S, Broholm C, Schefer J, et al. 2005. Magnetic inversion symmetry breaking and ferroelectricity in $TbMnO_3$. *Phys. Rev. Lett.* 95:087206
67. Katsura H, Nagaosa N, Balatsky AV. 2005. Spin current and magnetoelectric effect in noncollinear magnets. *Phys. Rev. Lett.* 95:057205
68. Sergienko IA, Dagotto E. 2006. Role of the Dzyaloshinskii-Moriya interaction in multiferroic perovskites. *Phys. Rev. B* 73:094434
69. Malashevich A, Vanderbilt D. 2008. First principles study of improper ferroelectricity in $TbMnO_3$. *Phys. Rev. Lett.* 101:037210
70. Mochizuki M, Nagaosa N. 2010. Theoretically predicted picosecond optical switching of spin chirality in multiferroics. *Phys. Rev. Lett.* 105:147202
71. Kubacka T, Johnson JA, Hoffmann MC, Vicario C, de Jong S, et al. 2014. Large-amplitude spin dynamics driven by a THz pulse in resonance with an electromagnon. *Science* 343:1333–36
72. Trigo M, Fuchs M, Chen J, Jiang MP, Cammarata M, et al. 2013. Fourier-transform inelastic X-ray scattering from time-and momentum-dependent phonon-phonon correlations. *Nat. Phys.* 9:790–94

73. Van Hove L. 1954. Correlations in space and time and born approximation scattering in systems of interacting particles. *Phys. Rev.* 95:249
74. Krisch M, Sette F. 2007. *Inelastic X-Ray Scattering from Phonons*. Berlin/Heidelberg: Springer
75. Baron AQR. 2014. *High-Resolution Inelastic X-Ray Scattering. I. Context, Spectrometers, Samples, and Superconductors*. Cham: Springer Int.
76. Baron AQR. 2014. *High-Resolution Inelastic X-Ray Scattering. II. Scattering Theory, Harmonic Phonons, and Calculations*. Cham: Springer Int.
77. Zhu D, Robert A, Henighan T, Lemke HT, Chollet M, et al. 2015. Phonon spectroscopy with sub-meV resolution by femtosecond X-ray diffuse scattering. *Phys. Rev. B* 92:054303
78. Garrett GA, Rojo AG, Sood AK, Whitaker JF, Merlin R. 1997. Vacuum squeezing of solids: macroscopic quantum states driven by light pulses. *Science* 275:1638–40
79. Johnson SL, Beaud P, Vorobeva E, Milne CJ, Murray ED, et al. 2009. Directly observing squeezed phonon states with femtosecond X-ray diffraction. *Phys. Rev. Lett.* 102:175503–4
80. Jiang MP, Trigo M, Savic I, Fahy S, Murray ED, et al. 2016. The origin of incipient ferroelectricity in lead telluride. *Nat. Commun.* 7:12291
81. Rousse A, Rischel C, Fourmaux S, Uschmann I, Sebban S, et al. 2001. Non-thermal melting in semiconductors measured at femtosecond resolution. *Nature* 410:65–68
82. Lindenberg AM, Kang I, Johnson SL, Missalla T, Heimann PA, et al. 2000. Time-resolved X-ray diffraction from coherent phonons during a laser-induced phase transition. *Phys. Rev. Lett.* 84:111–14
83. Shumay IL, Höfer U. 1996. Phase transformations of an InSb surface induced by strong femtosecond laser pulses. *Phys. Rev. B* 53:15878–84
84. Shank CV, Yen R, Hirlimann C. 1983. Time-resolved reflectivity measurements of femtosecond-optical-pulse-induced phase transitions in silicon. *Phys. Rev. Lett.* 50:454–57
85. Milathianaki D, Boutet S, Williams GJ, Higginbotham A, Ratner D, et al. 2013. Femtosecond visualization of lattice dynamics in shock-compressed matter. *Science* 342:220
86. Loveridge-Smith A, Allen A, Belak J, Boehly T, Hauer A, et al. 2001. Anomalous elastic response of silicon to uniaxial shock compression on nanosecond time scales. 86:2349–52
87. Lings B, Wark JS, DeCamp MF, Reis DA, Fahy S. 2006. Simulations of time-resolved X-ray diffraction in Laue geometry. *J. Phys. Condens. Matter* 18:9231–44
88. Szilagyi E, Wittenberg JS, Miller TA, Lutker K, Quirin F, et al. 2015. Visualization of nanocrystal breathing modes at extreme strains. *Nat. Commun.* 6:6577
89. Wittenberg JS, Miller TA, Szilagyi E, Lutker K, Quirin F, et al. 2014. Real-time visualization of nanocrystal solidsolid transformation pathways. *Nano Lett.* 14:1995–99
90. Turnbull D. 1950. Kinetics of heterogeneous nucleation. *J. Chem. Phys.* 18:198–203
91. Chen C, Herhold A, Johnson C, Alivisatos A. 1997. Size dependence of structural metastability in semiconductor nanocrystals. *Science* 276:398–401
92. Jacobs K, Zaziski D, Scher EC, Herhold EB, Alivisatos AP. 2001. Activation volumes for solid-solid transformations in nanocrystals. *Science* 293:1803–6
93. Grünwald M, Dellago C. 2009. Nucleation and growth in structural transformations of nanocrystals. *Nano Lett.* 9:2099–102
94. Morgan B, Madden P. 2006. Simulation of the pressure-driven wurtzite to rock salt phase transition in nanocrystals. *Phys. Chem. Chem. Phys.* 8:3304–13
95. Clark JN, Beitra L, Xiong G, Higginbotham A, Fritz DM, et al. 2013. Ultrafast three-dimensional imaging of lattice dynamics in individual gold nanocrystals. *Science* 341:56–59
96. Newton MC, Sao M, Fujisawa Y, Onitsuka R, Kawaguchi T, et al. 2014. Time-resolved coherent diffraction of ultrafast structural dynamics in a single nanowire. *Nano Lett.* 14:2413–18
97. Clark JN, Beitra L, Xiong G, Fritz DM, Lemke HT, et al. 2015. Imaging transient melting of a nanocrystal using an X-ray laser. *PNAS* 112:7444–48
98. Beaud P, Caviezel A, Mariager SO, Rettig L, Ingold G, et al. 2014. A time-dependent order parameter for ultrafast photoinduced phase transitions. *Nat. Mater.* 13:923–27
99. Mansart B, Cottet MJG, Mancini GF, Jarlborg T, Dugdale SB, et al. 2013. Temperature-dependent electron-phonon coupling in $La_{2-x}Sr_xCuO_4$ probed by femtosecond X-ray diffraction. *Phys. Rev. B* 88:054507

100. Mannebach EM, Li R, Duerloo KA, Nyby C, Zalden P, et al. 2015. Dynamic structural response and deformations of monolayer MoS_2 visualized by femtosecond electron diffraction. *Nano Lett.* 15:6889–95
101. Nie S, Wang X, Park H, Clinite R, Cao J. 2006. Measurement of the electronic Grüneisen constant using femtosecond electron diffraction. *Phys. Rev. Lett.* 96:025901
102. Singer A, Patel SKK, Kukreja R, Uhlíř V, Wingert J, et al. 2016. Photoinduced enhancement of the charge density wave amplitude. *Phys. Rev. Lett.* 117:056401
103. Daranciang D, Highland MJ, Wen H, Young SM, Brandt NC, et al. 2012. Ultrafast photovoltaic response in ferroelectric nanolayers. *Phys. Rev. Lett.* 108:087601
104. Wang RV, Fong DD, Jiang F, Highland MJ, Fuoss PH, et al. 2009. Reversible chemical switching of a ferroelectric film. *Phys. Rev. Lett.* 102:047601
105. Spanier JE, Kolpak AM, Urban JJ, Grinberg I, Ouyang L, et al. 2006. Ferroelectric phase transition in individual single-crystalline $BaTiO_3$ nanowires. *Nano Lett.* 6:735–39
106. Batra IP, Wurfel P, Silverman BD. 1973. Phase transition, stability, and depolarization field in ferroelectric thin films. *Phys. Rev. B* 8:3257–65
107. Lichtensteiger C, Triscone JM, Junquera J, Ghosez P. 2005. Ferroelectricity and tetragonality in ultrathin $PbTiO_3$ films. *Phys. Rev. Lett.* 94:047603
108. Yang SY, Seidel J, Byrnes SJ, Shafer P, Yang CH, et al. 2010. Above-bandgap voltages from ferroelectric photovoltaic devices. *Nat. Nanotechnol.* 5:143–47
109. Young S, Rappe A. 2012. First principles calculation of the shift current photovoltaic effect in ferroelectrics. *Phys. Rev. Lett.* 109:116601
110. Glass AM, Von der Linde D, Negran TJ. 1974. High-voltage bulk photovoltaic effect and the photorefractive process in $LiNbO_3$. *Appl. Phys. Lett.* 25:233–35
111. Fong DD, Kolpak AM, Eastman JA, Streiffer SK, Fuoss PH, et al. 2006. Stabilization of monodomain polarization in ultrathin $PbTiO_3$ films. *Phys. Rev. Lett.* 96:127601
112. Wen H, Chen P, Cosgriff MP, Walko DA, Lee JH, et al. 2013. Electronic origin of ultrafast photoinduced strain in $BiFeO_3$. *Phys. Rev. Lett.* 110:037601
113. Chen F, Zhu Y, Liu S, Qi Y, Hwang HY, et al. 2016. Ultrafast terahertz-field-driven ionic response in ferroelectric $BaTiO_3$. *Phys. Rev. B* 94:180104
114. Cohen MH, Falicov L, Golin S. 1964. Crystal chemistry and band structures of the group V semimetals and the IV–VI semiconductors. *IBM J. Res. Dev.* 8:215–27
115. Kawamura H. 1980. Phase transition in IV-VI compounds. In *Narrow Gap Semiconductors: Physics and Applications*, ed. W Zawadzki, pp. 470–94. Berlin: Springer
116. Zhang Y, Ke X, Kent PRC, Yang J, Chen C. 2011. Anomalous lattice dynamics near the ferroelectric instability in PbTe. *Phys. Rev. Lett.* 107:175503
117. Delaire O, Ma J, Marty K, May AF, McGuire MA, et al. 2011. Giant anharmonic phonon scattering in PbTe. *Nat. Mater.* 10:614–19
118. Jensen KM, Božin ES, Malliakas CD, Stone MB, Lumsden MD, et al. 2012. Lattice dynamics reveals a local symmetry breaking in the emergent dipole phase of PbTe. *Phys. Rev. B* 86:085313
119. Lee S, Esfarjani K, Luo T, Zhou J, Tian Z, Chen G. 2014. Resonant bonding leads to low lattice thermal conductivity. *Nat. Commun.* 5:3525
120. Newton MC, Sao M, Fujisawa Y, Onitsuka R, Kawaguchi T, et al. 2014. Time-resolved coherent diffraction of ultrafast structural dynamics in a single nanowire. *Nano Lett.* 14:2413–18
121. Ferguson KR, Bucher M, Gorkhover T, Boutet S, Fukuzawa H, et al. 2016. Transient lattice contraction in the solid-to-plasma transition. *Sci. Adv.* 2:e1500837
122. Ulvestad A, Singer A, Clark JN, Cho HM, Kim JW, et al. 2015. Topological defect dynamics in operando battery nanoparticles. *Science* 348:1344–47
123. Ulvestad A, Clark JN, Harder R, Robinson IK, Shpyrko OG. 2015. 3D imaging of twin domain defects in gold nanoparticles. *Nano Lett.* 15:4066–70
124. Robinson I, Clark J, Harder R. 2016. Materials science in the time domain using Bragg coherent diffraction imaging. *J. Opt.* 18:054007
125. Inoue I, Inubushi Y, Sato T, Tono K, Katayama T, et al. 2016. Observation of femtosecond X-ray interactions with matter using an X-ray–X-ray pump–probe scheme. *PNAS* 113:1492–97

126. Stephenson GB, Robert A, Grübel G. 2009. X-ray spectroscopy: revealing the atomic dance. *Nat. Mater.* 8:702–3
127. Alonso-Mori R, Caronna C, Chollet M, Curtis R, Damiani DS, et al. 2015. The X-ray Correlation Spectroscopy instrument at the Linac Coherent Light Source. *J. Synchrotron Radiat.* 22:508–13
128. Yabashi M, Tanaka H. 2017. The next ten years of X-ray science. *Nat. Photon.* 11:12–14
129. Billinge SJL, Levin I. 2007. The problem with determining atomic structure at the nanoscale. *Science* 316:561–65

Annual Review of
Materials Research

Volume 47, 2017

Contents

Novel Functionality Through Metamaterials (Venkatraman Gopalan, Don Lipkin & Simon Phillpot, Editors)

Control of Localized Surface Plasmon Resonances in Metal Oxide Nanocrystals
Ankit Agrawal, Robert W. Johns, and Delia J. Milliron 1

DNA-Driven Assembly: From Polyhedral Nanoparticles to Proteins
Martin Girard, Jaime A. Millan, and Monica Olvera de la Cruz 33

Harnessing Instabilities to Design Tunable Architected Cellular Materials
Katia Bertoldi 51

Negative-Poisson's-Ratio Materials: Auxetic Solids
Roderic S. Lakes 63

Sound Absorption Structures: From Porous Media to Acoustic Metamaterials
Min Yang and Ping Sheng 83

Structured X-Ray Optics for Laboratory-Based Materials Analysis
Carolyn A. MacDonald 115

Synchrotron X-Ray Optics
Albert T. Macrander and XianRong Huang 135

Current Interest

Active Crystal Growth Techniques for Quantum Materials
Julian L. Schmehr and Stephen D. Wilson 153

Atomic-Scale Structure-Property Relationships in Lithium Ion Battery Electrode Materials
Zhenzhong Yang, Lin Gu, Yong-Sheng Hu, and Hong Li 175

Atomistic Simulations of Activated Processes in Materials
G. Henkelman 199

Deformation of Crystals: Connections with Statistical Physics
James P. Sethna, Matthew K. Bierbaum, Karin A. Dahmen, Carl P. Goodrich, Julia R. Greer, Lorien X. Hayden, Jaron P. Kent-Dobias, Edward D. Lee, Danilo B. Liarte, Xiaoyue Ni, Katherine N. Quinn, Archishman Raju, D. Zeb Rocklin, Ashivni Shekhawat, and Stefano Zapperi 217

Heusler 4.0: Tunable Materials
Lukas Wollmann, Ajaya K. Nayak, Stuart S.P. Parkin, and Claudia Felser 247

Physical Dynamics of Ice Crystal Growth
Kenneth G. Libbrecht 271

Silicate Deposit Degradation of Engineered Coatings in Gas Turbines: Progress Toward Models and Materials Solutions
David L. Poerschke, R. Wesley Jackson, and Carlos G. Levi 297

Structural and Functional Fibers
Huibin Chang, Jeffrey Luo, Prabhakar V. Gulgunje, and Satish Kumar 331

Synthetic Two-Dimensional Polymers
Marco Servalli and A. Dieter Schlüter 361

Transparent Perovskite Barium Stannate with High Electron Mobility and Thermal Stability
Woong-Jhae Lee, Hyung Joon Kim, Jeonghun Kang, Dong Hyun Jang, Tai Hoon Kim, Jeong Hyuk Lee, and Kee Hoon Kim 391

Visualization of Atomic-Scale Motions in Materials via Femtosecond X-Ray Scattering Techniques
Aaron M. Lindenberg, Steven L. Johnson, and David A. Reis 425

X-Ray Tomography for Lithium Ion Battery Research: A Practical Guide
Patrick Pietsch and Vanessa Wood 451

Indexes

Cumulative Index of Contributing Authors, Volumes 43–47 481

Errata

An online log of corrections to *Annual Review of Materials Research* articles may be found at http://www.annualreviews.org/errata/matsci